Local Hydrodynamics in a Dispersed-Stratified Liquid–Liquid Pipe Flow

C. Conan
Laboratoire de Génie Chimique, UMR 5503 CNRS/INPT/UPS, 31106 Toulouse Cedex 1, France,
and IFP, Dept. de Mécanique Appliquée, 1 et 4 Av. de Bois-Préau, 92852 Rueil-Malmaison, France

O. Masbernat
Laboratoire de Génie Chimique, UMR 5503 CNRS/INPT/UPS, 31106 Toulouse Cedex 1, France

S. Décarre
IFP, Dept. de Mécanique Appliquée, 1 et 4 Av. de Bois-Préau, 92852 Rueil-Malmaison, France

A. Liné
Laboratoire d'Ingénierie des Systèmes Biologiques et des Procédés, UMR INSA-CNRS 5504,
UMR INSA-INRA 792, F-31077 Toulouse Cedex 4, France

DOI 10.1002/aic.11309

An experimental study is presented of a liquid–liquid dispersed/stratified flow in a horizontal pipe. The flow studied contains a highly concentrated layer of oil drops (light phase) under which flows a continuous layer of aqueous phase (heavy phase). The instant flow structure and hydrodynamics have been characterized in the aqueous phase using Particle Image Velocimetry in a matched refractive index medium. In this article, we focus on momentum transfer in the continuous aqueous layer at the wall, and at the interface, between the aqueous layer and the concentrated layer of oil drops. It is shown that, despite the presence of secondary flows, the velocity profile in the aqueous phase follows the classical logarithmic law near the wall. The shape of the tangential Reynolds stress profile in the aqueous layer is discussed in relation with the flow geometry and the presence of secondary flows. The mean interfacial shear stress is then derived from the macroscopic momentum balance applied in the aqueous layer cross-section. The local viscous stress contribution below the interface has been identified from the momentum balance equation in the vertical direction and an effective viscosity as a function of the local concentration has been derived. © 2007 American Institute of Chemical Engineers *AIChE J,* 53: 2754–2768, 2007
Keywords: liquid–liquid stratified/dispersed flows, PIV, wall shear stress, interfacial shear stress, secondary flows, turbulence

Introduction

In petroleum recovery industry, oil extraction is often accompanied with a high water throughput, increasing as the drilling site is aging (up to 50% in volumetric fraction). In the last decade, the drilling of horizontal or nearly horizontal wells has been developed, reducing production costs and environmental impact. This evolution of drilling techniques has raised the interest for studying liquid–liquid flows in horizontal pipes.

Experimental studies of these flows have shown that two immiscible liquid phases (oil and water) flowing co-currently

---

Correspondence concerning this article should be addressed to A. Liné at alain.line@insa-toulouse.fr.

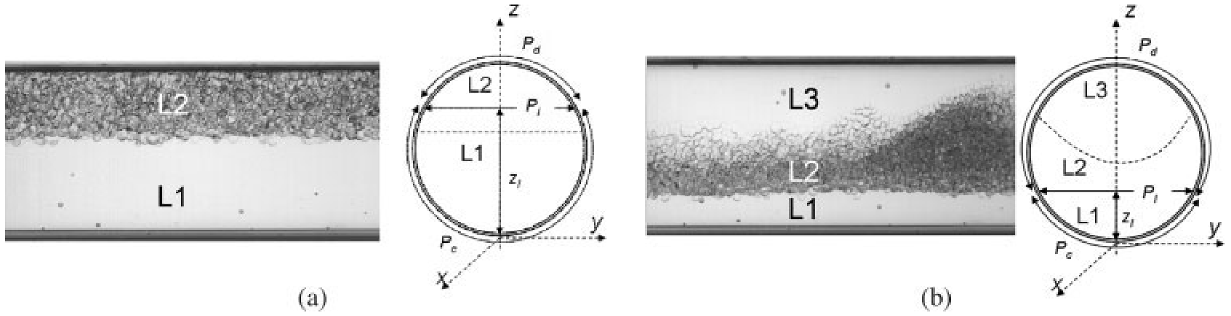

Figure 1. Structure of the stratified-dispersed flow (a) 2-layer flow with L1, the layer of continuous water and L2, the layer of oil drops in water; (b) 3-layer flow. L3 is a continuous layer of oil.

in a horizontal pipe can take different spatial configurations according to the total flow rate (or mixture velocity) and to the phase ratio (or volume fraction) (e.g. see Arirachakaran et al.[1]; Nädler and Mewes[2]; Angeli and Hewitt[3]; Elseth[4] Rodriguez et al.[5]). The transition and boundaries between these regimes seem to depend upon the oil-water system physical properties but also on the duct material.[3] Theoretical works addressing this problem (Brauner and Moalem-Maron[6]; Trallero[7]; Brauner[8]; Chakrabarti et al.[9]) have also to be mentioned. The local hydrodynamics characteristics being closely related to the flow pattern, the modeling of these flow regimes must be addressed separately. These flow regimes can be displayed on a mixture velocity/watercut map from which three main configurations can be distinguished:

Fully separated flow (or stratified): This regime occurs at low value of mixture velocity. Both liquids flow in the pipe separated by a continuous interface (the heaviest below the lightest). Prediction of the pressure drop in these flows requires the knowledge of wall shear stress in both phases as well as the interfacial shear stress. In stratified gas-liquid flows, Liné and Fabre[10] have shown that the wall friction factor is well predicted for both phases by the classical single-phase flow relations provided that the liquid fraction is not too small. The interfacial friction factor is defined as a wall friction factor with a Reynolds number based on the relative velocity between both phases. The presence of the waves at the interface can be modeled by considering the wavy interface as a rough wall. In the case of liquid–liquid flows, Elseth[4] showed that a classical two-fluid model also gives good pressure drop and phase hold-up predictions, even when waves develop at the interface. The interfacial friction factor used was the Haaland friction factor with a roughness set to zero, reducing to Blasius law. In fact, if the interfacial shear stress is an important issue with respect to the modeling of pressure drop and phase hold-ups in gas-liquid flows, its influence is considerably reduced in oil-water pipe flows, due to the closeness of density and viscosity of both liquids. In this case, compared to the mixture velocity, the slip velocity is weak for a wide range of input volume fractions (or flow rate ratios), and the interfacial friction is small before the wall friction.

Fully dispersed flow: At high values of the mixture velocity, the destabilization of the interface (enhanced by the presence of restrictions, valves or any accidents in the pipe) results in the formation of drops which are distributed in the whole pipe section (with a vertical gradient of concentration more or less pronounced). The fully dispersed regime occurs when the turbulent kinetic energy level is strong enough to counterbalance the buoyancy force and to maintain a suspension of drops in the bulk flow. In terms of modeling, fully dispersed liquid–liquid flow involves new questions related to two phenomena, (i) turbulence damping of the carrier phase due to the drops and (ii) increase of the apparent viscosity of the mixture (the latter is the preponderant phenomenon when the concentration in drops is high).

Stratified/dispersed flow: It is a stratified flow with a confined dense dispersed layer. This flow regime occurs at intermediate mixture velocities. The phase distribution is controlled by the buoyancy force and the light dispersed phase forms a highly concentrated dispersion entrained by the water phase. Few data about this flow regime are available in the literature and the evolution of the pressure drop as a function of the phase fraction and velocity is not fully understood (Elseth[4]).

The objective of the present work is to provide detailed data on the local structure of the stratified-dispersed flow of two immiscible liquids (oil and water). The stratified/dispersed flow studied is generated at the pipe inlet thanks to a network of capillary tubes which provides a nearly monodispersed distribution of oil drops. A stable stratified regime develops from the inlet section. It is composed of 2 or 3 layers, depending on the inlet oil-water ratio. Global views of these two different regimes are illustrated in Figures 1a, b (*n*-heptane dispersed in water). The lower part of the pipe cross-section is occupied by a layer of water L1 and the upper part by a dense layer of oil drops L2 dispersed in water. A third layer L3, resulting of a coalescence process at the pipe inlet may appear at higher input oil volume fraction.

This flow pattern raises original problems in terms of multiphase flow modeling. Among those, an important question is the ability of the stratified flow model to represent this flow regime. Assuming the flow to be fully developed (in x-direction), the integrated momentum balance in layer L1 (water phase) reads:

$$\frac{dp}{dx}A_{\mathrm{c}} = \overline{\tau_{\mathrm{c}}}P_{\mathrm{c}} + \overline{\tau_{\mathrm{I}}}P_{\mathrm{I}} \tag{1}$$

where $\overline{\tau_{\mathrm{c}}}$ and $\overline{\tau_{\mathrm{I}}}$ are respectively the wall and interfacial shear stresses in the aqueous phase. In this model, the boundary between layers L1 and L2 is assumed to be horizontal in average and its vertical position is noted z_{I} (the origin of z axis is fixed at the bottom of the pipe). In Eq. 1, interfacial mean shear stress $\overline{\tau_{\mathrm{I}}}$ is evaluated at $z = z_{\mathrm{I}}$. P_{I}, P_{c} and A_{c} (defined

Table 1. Physical Properties of Liquid–Liquid System at $T = 29°C$

	Liquid Phase	ρ (kg/m^3)	μ (Pa s)	σ (N/m)	n_D
Dispersed	Heptane	684	4.5×10^{-4}	31×10^{-3}	1.3909
Continuous	Water + glycerine (50 vol %)	1123	4.2×10^{-3}		1.3900

in Figure 1) are respectively the interfacial perimeter (between L1 and L2), the wall perimeter wetted by the aqueous phase and the cross section of the aqueous phase flow (L1 layer). These geometrical parameters can be related to the angle Ω which is defined by the position of the interface between the continuous phase and the dense dispersed phase (Figure 12).

$$\frac{A_c}{A} = \frac{\Omega - \sin\Omega}{2\pi}, P_c = \Omega\frac{D}{2}, P_I = D\sin\frac{\Omega}{2}, \quad z_I = \frac{D}{2}\left(1 - \cos\frac{\Omega}{2}\right) \qquad (2)$$

Once the position of the interface z_I is known (or the angle Ω), the other geometrical parameters are known. Therefore, the first question to be addressed is the existence and the definition of this interface in such kind of flow. The second question concerns the evaluation of the wall shear stress in the continuous heavy phase, $\overline{\tau_c}$, and its evolution with the flow mean velocity in the L2 layer. The local structure of the turbulence near the wall and the wall friction velocity along the wetted perimeter needs to be characterized, as well as the influence of the dispersed oil layer on the continuous phase hydrodynamics.

The last point to be addressed in view of modeling the pressure drop gradient along the longitudinal direction is the interfacial shear stress $\overline{\tau_I}$, the global shear stress of the continuous phase exerted at $z = z_I$. If, as mentioned above, in fully separated liquid–liquid flow, the influence of $\overline{\tau_I}$ is expected to be weak, in stratified-dispersed flow, the presence of a dense layer of drops at the interface may significantly increase its relative weight in the momentum balance.

In this article, we focus on the local hydrodynamics of the heaviest phase (aqueous solution) in the continuous layer (L1). In that aim, Particle Image Velocimetry (PIV) measurements have been achieved in the aqueous phase for a liquid–liquid system with matched refractive indices (*n*-heptane dispersed in a water-glycerine mixture). The paper is structured as follows: in *experimental* section, the experimental device and the measurement techniques are presented. The mean flow structure is discussed in the *Mean Flow Field in L1 Layer* section and the wall turbulence in the aqueous phase is analyzed in the *Wall Turbulence in the L1 Layer* section. The interfacial shear stress is studied in the *interfacial shear stress* section, at a global scale (deduced from Eq. 1) and at a local scale from the momentum transport equation. Main results are summarized in the last section.

Experimental

Phase system

The dispersed phase is *n*-heptane (purity 96%) and the continuous phase is a mixture (~50% in volume) of tap water and glycerine. The physical properties of these fluids are given in Table 1 at a temperature of 29°C (operating temperature).

Experimental device

A schematic diagram of the liquid–liquid loop is shown in Figure 2. The experimental device consists of a horizontal co-current dispersed liquid–liquid flow in an 8 m long cylindrical pipe with a 5 cm diameter. This duct is made up of four 2 m long removable sections. In view of implementing optical techniques, the duct material is a transparent polymer (poly-methyl-metacrylate). To reduce optical distortions, a movable 30 cm long square section box filled with distilled water, is mounted on each section of the pipe.

The continuous phase enters the duct via a stainless steel conic convergent section and the dispersed phase is introduced co-currently through 673 stainless steel capillary tubes of 1 mm inner diameter, mounted inside the convergent section. The number of capillary tubes was chosen in order to provide a maximum flow rate of 6 m^3/h with a velocity inside the capillary tubes smaller than 3 m/s (in order to avoid pulverization). Thus, in most of the cases, the drop formation results from regular jet break-up at the exit of the capillary tubes. The resulting dispersion exhibits a narrow size distribution with an average diameter ranging between 2 and 4 mm, depending on both the continuous phase and the dispersed phase flow rates. Finally, the two phases are continuously separated in a 400 L box settler and sent back to the duct entry section by centrifugal pumps of variable rotation speed.

A secondary heated water loop allows the temperature control in the duct. The temperature is regulated with a precision of 0.1°C thanks to a heat exchanger. The operating temperature of all experiments has been set to 29°C.

Pressure drop measurements

Pressure taps have been mounted on each section of the duct (every 2 m) and are related to a differential pressure

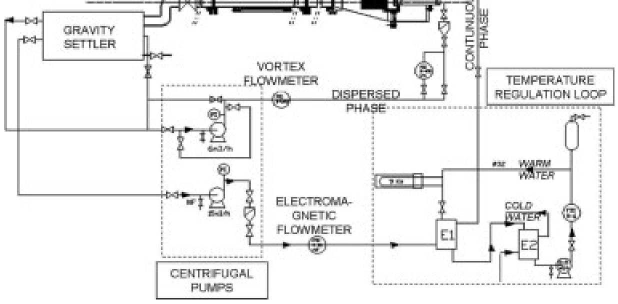

Figure 2. Scheme of the liquid–liquid flow loop facility.

gauge. The instantaneous pressure signal is time-averaged and for each flowrate studied, its longitudinal gradient is stable along the pipe length in both single and two-phase flow. Its variation with the mixture velocity and inlet phase ratio will not be discussed in this article.

Particle image velocimetry

A high speed PIV technique was developed to measure the local instant 2-dimensional velocity fields of the aqueous phase. The principle of this technique is to measure the displacement of small seeding particles (behaving as flow tracers) between two successive recorded images of the flow.

In the present case, a 1024 × 1024 pixels^2 image size has been used which approximately corresponds to a 50 × 50 mm^2 flow section. Fluorescent particles made of poly methyl-methacrylate (pmma) were used to seed the flow. Their diameter ranges between 1 and 20 μm. A 2 × 10 mJ dual head laser Nd:YLF PEGASUS ($\lambda = 527$ nm) was used to generate a thin pulsed laser sheet (1 kHz) in a median plane along the longitudinal axis of the duct. The time between two pulses was taken as large as possible for the calculation of statistical averages. The duration of each laser flash is less than 180 ns, avoiding any fuzzy effect due to the particle motion. The use of a pass-band filter mounted on the camera objective enabled to collect the light only issued from the fluorescent μ-particles, eliminating all the parasite light reflections from the walls (duct wall, square box walls). Recorded images were divided into square interrogation windows, within which the grey level cross-correlation function between two consecutive images is calculated along the vertical and transverse directions. The coordinates of the maximum peak of the cross-correlation give the most probable displacement of the flow in one interrogation window. The accuracy of the result was enhanced by a Gaussian interpolation of the resulting cross-correlation peaks and by the application of iterative calculation procedures, combining spatial shift and size reduction of interrogation windows (from 64 × 64 to 32 × 32 px^2 or 16 × 16 px^2 depending on the μ-particle concentration). The velocity of the continuous phase was processed using the software DaVis 7.0. More details about these techniques can be found in Raffel et al.[11] and Fincham and Delerce.[12]

Single phase flow measurements

The velocity field PIV measurement has been first validated with a single phase flow of water–glycerin mixture. For mean velocities larger than 0.15 m/s ($Re_m > 2000$), it was verified that the flow was established since the 2nd test section (2.5 m downstream of the inlet section). Calculated mean velocities (not shown in this paper) verify the classical turbulent behaviors (logarithmic law in the inertial layer and linear law in the viscous layer) as well as the second order momentum ($\overline{v_x^2}$, $\overline{v_r^2}$ and $\overline{v_x v_r}$) which are in good agreement with Laufer[13] measurements. Pressure losses estimated thanks to the linear behavior of the crossed velocity correlations $\overline{v_x v_r}$ in the inertial area, are in good agreement with differential pressure gauge data.

Two-phase flow measurements

Application of PIV measurements in dispersed liquid–liquid flows is made possible thanks to the refractive indices matching of both phases as already shown by Augier et al.[14] and Galinat[15] (see also Adrian[16] in solid–liquid flows). This method avoids laser sheet reflections due to the crossing of drop interfaces that would generate shadow areas in the images. The pmma micro-particles used in the present study are mostly hydrophilic. These particles are only present in the aqueous continuous phase and do not diffuse in the organic dispersed phase. As a consequence, drops appear as "black" holes in the recorded images. The evaluation of cross-correlations in the dense dispersed layer needs particular care because of the low number density of particles, responsible of significant bias in the calculation of the velocity. The filtering of low signal-to-noise ratio correlation peaks as well as that of very low velocities has been applied in order to remove erroneous instant values. Estimation of mean fields therefore needs a higher number of instantaneous fields (more than 1000 samples) in order to ensure the convergence of statistical average. In particular, in the 3-layer regime, the rate of convergence near the L2-L3 interface is very low due to concentration waves of the dense dispersed layer.

Flow parameters

The experimental test cases for both systems are reported in Table 2. Inlet oil ratio ϕ_o and mixture velocity U_m are defined as:

$$\phi_o = \frac{Q_o}{Q_o + Q_w} \tag{3}$$

$$Q_t = Q_o + Q_w \tag{4}$$

$$U_m = \frac{Q_t}{A} \tag{5}$$

where Q_w (respectively Q_o) is the water–glycerine (respectively oil) phase flow rate in the pipe and A is the pipe section area. The mixture velocity ranges from 0.28 to 1.2 m/s and the input oil ratio ϕ_o ranges from 0.025 to 0.85 (the inlet ratio is limited by the box settler separation capacity and by the maximum oil flow rate).

In the next sections, two test cases have been selected to illustrate the vertical and horizontal profiles of mean and turbulent quantities in the L1 layer: ($U_m = 0.57$ m/s; $\phi_o = 0.1$) and ($U_m = 0.57$ m/s; $\phi_o = 0.2$), which correspond to a 2-layer and a 3-layer regime, respectively. All profiles presented have been recorded in the 2nd measuring section, at 3 m from the flow inlet section. The flow pattern and velocity field have been checked to be stable and established at this distance from the entry section.

Mean Flow Field in L1 Layer

Vertical profiles

Longitudinal normalized mean velocity V_x and continuous phase hold-up α_w profiles in the median vertical plane are displayed for both test cases in Figures 3a and 3b. The corresponding flow pattern has been also reported (raw images on the right of the figures).

Water hold-up profiles (α_w) have been obtained after averaging the grey level over a large sample of images (>1000

Table 2. Studied Flow Cases and Corresponding Data

Flow Regime	Q_t (m^3/h)	ϕ_o	U_m (m/s)	z_I/D	$-dp/dx$ (Pa/m)	$\overline{\tau_c}$ (Pa)	$\overline{\tau_I}$ (Pa)	τ_{Iloc} (Pa)
2 Layers	2	0.06	0.28	0.74	132	0.8	3.2	2.0
	2	0.11	0.28	0.64	180	1.1	3.2	1.4
	3	0.05	0.42	0.77	178	1.4	3.8	2.8
	3	0.15	0.42	0.70	163	1.4	2.6	1.7
	4	0.05	0.57	0.86	206	2.0	5.0	3.4
	4	0.11	0.57	0.84	242	2.2	6.6	5.2
	6	0.05	0.85	0.88	308	3.3	5.3	4.7
	6	0.10	0.85	0.85	342	3.6	6.9	4.5
	6	0.20	0.85	0.66	402	5.5	3.3	5.2
	12	0.11	1.73	0.98	512	–	–	–
3 Layers	2	0.22	0.28	0.60	127	0.9	1.8	1.4
	2	0.40	0.28	0.47	157	0.9	1.6	1.2
	2	0.51	0.28	0.40	135	0.9	0.7	0.8
	2	0.60	0.28	0.35	136	1.0	3.5	0.8
	3	0.20	0.42	0.63	144	1.3	1.3	1.6
	3	0.30	0.42	0.54	150	1.5	0.7	1.7
	3	0.40	0.42	0.47	170	1.5	0.6	1.1
	4	0.20	0.57	0.65	216	2.2	2.0	2.8
	4	0.40	0.57	0.54	211	2.2	1.3	2.0
	4	0.50	0.57	0.46	236	2.2	1.0	3.3
	4	0.70	0.57	0.29	179	2.0	–	0.2

images) and after application of a threshold. These profiles are truncated near the walls to filter the artefacts due to the accumulation of μ-particles along the wall. Even if these hold-up profiles are qualitative, they characterize the transition between L1 and L2 layers. We note that the water hold-up gradient is more pronounced at $\phi_o = 0.2$ than at $\phi_o = 0.1$. This is due to the drop re-entrainment by the continuous phase, observed at low ϕ_o. The quasi hexagonal shape of the drops in the L2 layer indicates that the local oil volume fraction probably reaches values as high as 90% and more in the core of the dense dispersed layer L2.

The longitudinal velocity profiles in the aqueous phase ($\alpha_w = 1$) have similar shapes in both cases, exhibiting a maximum always contained in the aqueous phase. In return,

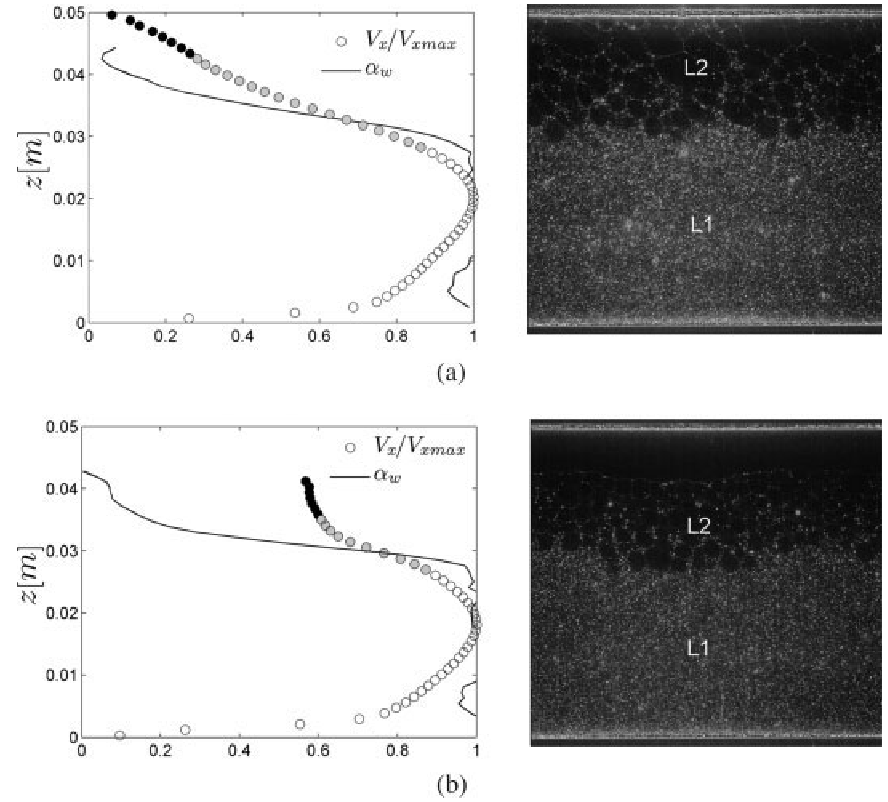

Figure 3. Vertical profiles of the longitudinal velocity and water phase hold-up U_m = 0.57 m/s; (a) ϕ_o = 0.1; (b) ϕ_o = 0.2.

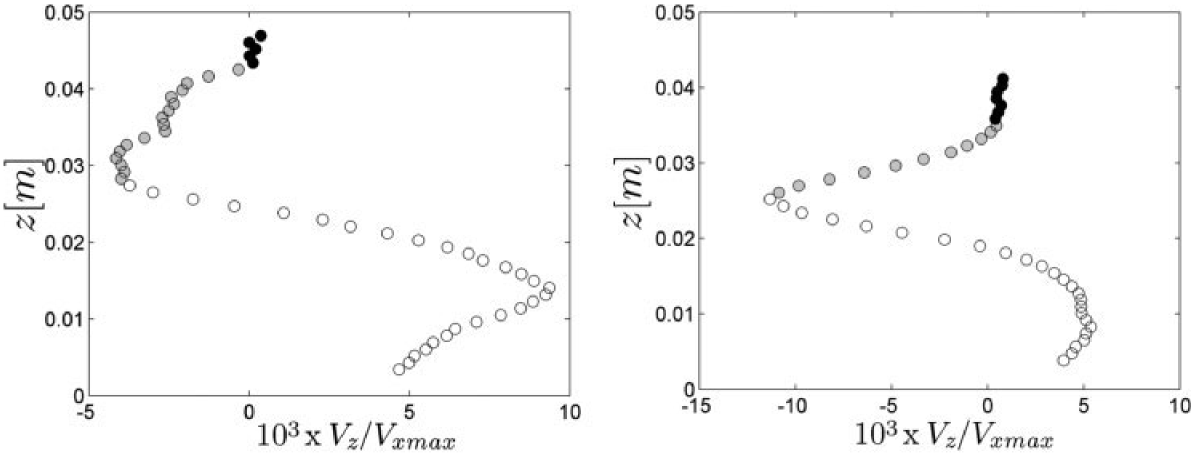

(a) (b)

Figure 4. Vertical profile of the mean vertical velocity: (a) $\phi_o = 0.1$. (b) $\phi_o = 0.2$. $U_m = 0.57$ m/s.

the shape of the profiles in the dispersed layer differs between the 2-layer (Figure 3a) and the 3-layer regime (Figure 3b). In the 2-layer regime the vertical gradient is much more pronounced than in the 3-layer regime where the velocity is more uniform in the dense layer.

Vertical profiles of mean normalized vertical velocity V_z have been reported in Figures 4a and 4b for both selected test cases. The intensity of this velocity component does not exceed 1% of the maximum longitudinal velocity $V_{x\max}$ but is large enough to be accounted for in the momentum balance. Three distinct zones can be distinguished on these profiles: white symbols correspond to the measurements performed in the continuous aqueous layer ($\alpha_w = 1$). Grey circles correspond to a transition zone, where oil drops are present in the water flow (this zone is characterized in Figure 3a and 3b by an abrupt decrease of α_w), but their concentration is not high enough to avoid vertical displacements of the aqueous phase. Finally, black circles correspond to the measurements in the dense dispersed layer above the location where the vertical velocity cancels. Note that this position also corresponds to the location where the velocity fluctuation cross correlation measured in water is equal to zero (see Figure 9).

Horizontal profiles

Horizontal profiles of longitudinal normalized velocity $V_x/V_{x\max}$ have been plotted in Figure 5a. These profiles have been measured in both test cases a few millimeters below the dispersed layer, in a median horizontal plane of the pipe fully occupied by the aqueous phase ($\alpha_w = 1$). The flat shape of these profiles is remarkable. It probably results from the particular rheology of the dense dispersed layer which behaves as a "solid" in the horizontal plane. The shape of iso-value contours of longitudinal velocity V_x deduced from the vertical and horizontal profiles (Figures 3 and 5a) is sketched in Figure 6b. Hence, in the L1-L2 transition zone, only the vertical derivative of the longitudinal velocity is different from zero.

Another possible explanation to the flat horizontal profile of V_x below the L2 layer might be due to the presence of

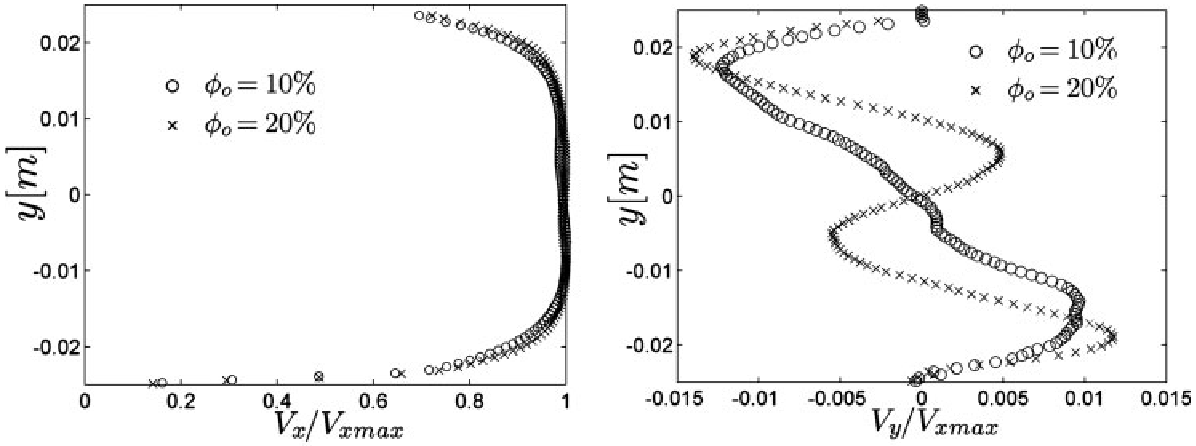

(a) (b)

Figure 5. (a) Horizontal profile of the longitudinal velocity below layer L2; (b) horizontal profile of the mean transverse velocity; $U_m = 0.57$ m/s.

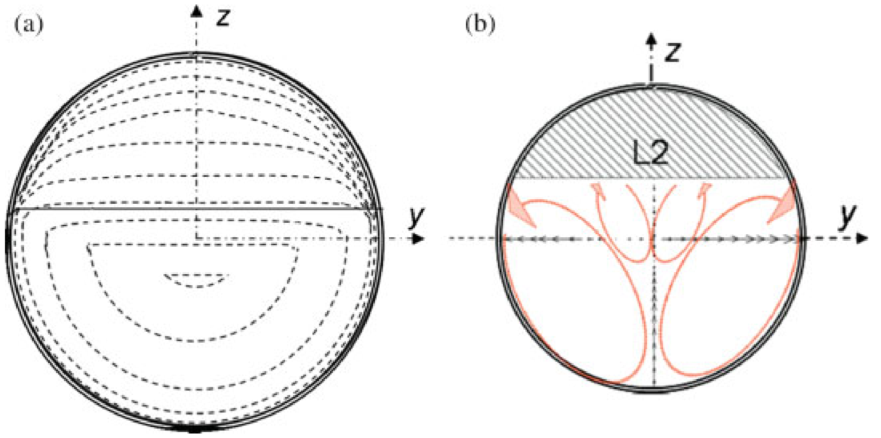

Figure 6. (a) velocity contours in the pipe cross section (b) Secondary flow structures deduced from radial velocity measurements (U_m = 0.57 m/s, ϕ_o = 0.1).

[Color figure can be viewed in the online issue, which is available at www.interscience.wiley.com.]

secondary flows in L1 layer. Such secondary flows are known to modify the structure of the longitudinal velocity in gas–liquid stratified flows (Liné et al.,[17] Meknassi et al.[18]). Figure 5b shows the horizontal profile of normalized mean transverse velocity V_y. The intensity of the horizontal component lies in the same range as that of the vertical component (<1% of the maximum longitudinal velocity) and the symmetry observed with respect to the center of the pipe section is the signature of secondary flow vortices.

Secondary flow structures

The presence of secondary flows has been clearly demonstrated from the horizontal profile of transverse component V_y (Figure 5b) and vertical profile of vertical component V_z (Figure 4). The structure of these flows is schematized in Figure 6b. It is composed of two symmetrical pairs of counter-rotating vortices, the size of which depends on the flow configuration (2 or 3 layers).

This structure is similar to that already observed in the gas phase by Liné et al.[17] and Meknassi et al.[18] in stratified gas–liquid flow. In this case, a pair of vortices is observed in the corner bordered by the wall and the interface. Interestingly, these authors found that increasing the gas velocity was changing the relative size of the vortices, a result attributed to the nonuniform stress distribution along the gas phase perimeter (highlighted by Hinze[19] in experiments on channel flows with non uniform roughness). Although not studied in details, such a mechanism seems to take place in the present flow, the aqueous phase substituting to the gas phase.

Secondary flows are related to the anisotropy of the turbulence. Transport equation of longitudinal vorticity $\overline{\Omega_x}$ $(=\frac{\partial\overline{V_z}}{\partial y}-\frac{\partial\overline{V_y}}{\partial z})$ reads:

$$\overline{V_y}\frac{\partial\overline{\Omega_x}}{\partial y}+\overline{V_z}\frac{\partial\overline{\Omega_x}}{\partial z}=\frac{\partial^2}{\partial y\partial z}\left(\overline{w'^2}-\overline{v'^2}\right)+\left(\frac{\partial^2}{\partial y^2}-\frac{\partial^2}{\partial z^2}\right)\overline{v'w'}+\nu\left(\frac{\partial^2\overline{\Omega_x}}{\partial y^2}+\frac{\partial^2\overline{\Omega_x}}{\partial z^2}\right) \qquad (6)$$

In the stratified-dispersed flow studied, secondary flows probably originate from the non uniformity of turbulent kinetic energy along the perimeter of the continuous phase, in particular along the wall and below the interface.

Location of L1-L2 interface

Unlike fully separated flows, the transition between the flow layers is not clearly defined by the presence of a continuous interface. The finite thickness of the hold-up gradient observed in this zone (Figure 3) defines a range of vertical location of the L1-L2 boundary, and not an accurate position of the interface (noted z_I). A first simple criterion is to arbitrarily define the interface location as the mean "first drop position" z_e, that is, the vertical coordinate above which the mean water hold-up α_w begins to decrease. In this case, the L1 layer is a single phase flow zone, occupied by the aqueous phase. However, as aforementioned, due to the presence of secondary flows, vertical velocities are not equal to zero at that position, they are even close to their maximum value. In these conditions, the validity of Eq. 1 is questionable. Hence, a more rigorous definition of the thickness of the continuous water layer z_I, is the vertical distance at which the vertical velocity cancels. This location has been determined thanks to PIV measurements, and was found to also correspond to the position where cross-correlation of fluctuating velocity, $\overline{v_x v_z}$, tends towards zero (cf. Figure 9). Above z_I, the structure is so dense (the oil hold-up is higher than 0.9 ($\alpha_w < 0.1$)) that it is impermeable to the water phase. With this definition of the interface, the L1 layer is no longer a single phase flow region. It is composed of two zones: a first section only occupied by the continuous phase, ranging from the pipe bottom up to the "first drop" position ($0 < z < z_e$), and a section comprised between z_e and the interface position z_I. In the second, oil drops are present, but the integrated momentum balance (Eq. 1) can be applied.

The thickness z_I has been determined from PIV measurements for test cases of Table 2, and correlated to the input oil ratio ϕ_o and mixture velocity U_m. As illustrated in Figure 7,

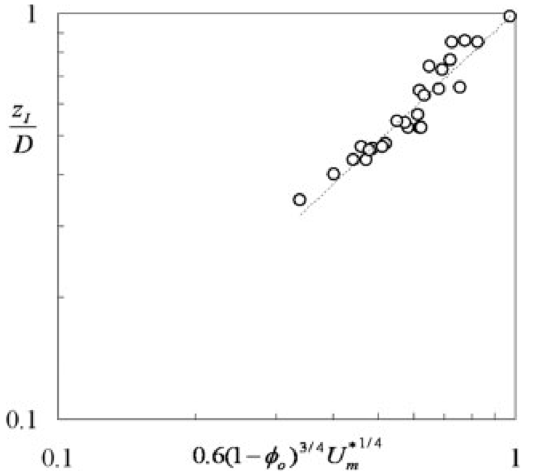

Figure 7. Vertical position of L1-L2 boundary z_I/D as a function of inlet oil ratio ϕ_o and mixture velocity U^*_m.

Theoretical expression of z_I/D in case of a fully separated stratified flow with zero slip velocity condition is: $(z_I/D)_{\text{Noslip}} \equiv 0.9(1-\phi_o)^{3/4}$.

experimental data well regroup around the following relation:

$$\frac{z_I}{D} = 0.6(1-\phi_o)^{3/4}U_m^{*1/4} \tag{7}$$

In the above correlation, U^*_m is the mixture velocity normalized by $\sqrt{gd}$ (d is the drop diameter). Note that this relation doesn't depend of the flow configuration (2 or 3 layers) and can be compared with the theoretical case of a fully separated liquid–liquid flow with a no-slip condition at the interface. Assuming this L1-L2 interface to be horizontal, the cross section of the aqueous phase can be determined from the only parameter z_I:

$$\begin{aligned} 1-\phi_o &= \frac{A_c}{A} \\ &= \frac{1}{\pi}\left[\pi - \cos^{-1}\left(\frac{z_I-R}{R}\right) - \frac{1}{2}\sqrt{1-\left(\frac{z_I-R}{R}\right)^2}\,\right] \end{aligned} \tag{8}$$

This geometrical relation can be approximated with a good accuracy by the following relation:

$$\left(\frac{z_I}{D}\right)_{\text{no-slip}} = 0.9(1-\phi_o)^{3/4} \quad \text{for } 0.05 < \phi_o < 0.95 \tag{9}$$

Compared to relation (9), correlation (7) indicates that the hydrodynamic interface position of the stratified-dispersed flow is a simple geometrical relation slightly weighted by the mixture velocity.

Wall Turbulence in the L1 Layer

With the objective of determining closure relations for the global momentum transfer in the L1 layer at the wall, wall turbulence has been investigated, starting with the mean longitudinal velocity profile in the wall region.

Log-law velocity profile

Following Liné et al.[17] and Wang and Cheng,[20] the near wall longitudinal velocity is assumed to be unaffected by the presence of secondary flows. The wall friction velocity v^* has been estimated from the classical logarithmic law in the inertial region:

$$V^+ = \frac{1}{\kappa}\ln z^+ + B \tag{10}$$

where $V^+ = V_x/v^*$ and $z^+ = \frac{zv^*}{\mu_c/\rho_c}$, $\kappa = 0.41$ and $B = 5.5$ ($\kappa = 0.41$ and $B = 5.5$ are single phase flow values in circular pipes). μ_c/ρ_c is the kinematic viscosity of the aqueous phase. The friction velocity is defined as

$$v^* = \sqrt{\frac{\overline{\tau_c}}{\rho_c}} \tag{11}$$

where $\overline{\tau_c}$ is the wall shear stress. Figure 8a reports the normalized longitudinal velocity V^+ as a function of the normalized distance from the wall z^+, for both test cases (U_m = 0.57 m/s; ϕ_o = 0.1 and 0.2) and for single phase flow case ((U_m = 0.57 m/s; ϕ_o = 0). Reynolds number defined in the aqueous phase section ($z < z_I$) ranges between 7000 and

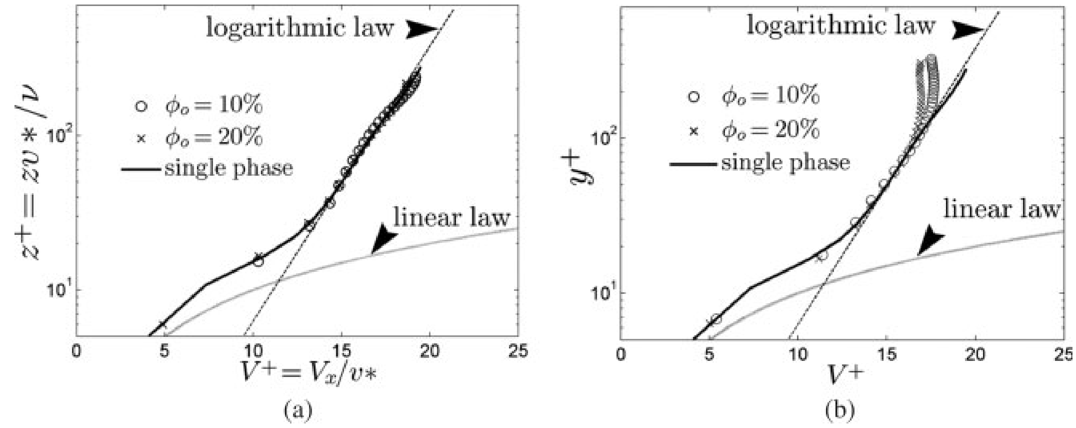

Figure 8. (a) Vertical and (b) horizontal axial velocity profiles in the near wall region.

Table 3. Mean Wall Stress Velocities v^* Estimated From Horizontal and Vertical Velocity Profiles

ϕ_o	v^* (horiz.) (m/s)	v^* (vert.) (m/s)
0.2	0.042	0.044
0.1	0.044	0.045
0.05	0.044	0.043

8000. In the presented cases the universal logarithmic profile is valid up to $z^+ = 150 - 170$. The linear law $V^+ = z^+$, in the viscous sublayer, is also well verified for $z^+ < 10$. In all studied cases, the logarithmic law applies from $z^+ = 30$ (which is similar to single phase flow case).

In the same way, the wall friction velocity has been evaluated in the median horizontal plane below the dispersed layer. Horizontal normalized profiles of mean longitudinal velocity in the wall region are displayed in Figure 8b. The logarithmic law is still reproduced near the wall and is valid from $y^+ = 30$ up to $y^+ = 150$. At larger y^+, the velocity profile is below the log-law which probably results from the damping of turbulence by the dispersed layer. Table 3 reports the values of the friction velocity estimated in the same input conditions ($U_m = 0.57$ m/s) from both horizontal and vertical profiles. The small differences observed allow to consider the wall friction as being constant along the aqueous phase wetted perimeter. It can be therefore concluded that the local wall shear stress, determined from the measurements in the vertical plane ($z = 0$, $y = 0$), is representative of $\overline{\tau_c}$, the mean wall shear stress of layer L1.

Turbulence profiles

The longitudinal and vertical fluctuating velocities have been measured as well as the transverse velocity component (not reported here). Ratios $\sqrt{\overline{v_x'^2}}/v^*$ and $\sqrt{\overline{v_z'^2}}/v^*$ estimated from vertical profiles and $\sqrt{\overline{v_y'^2}}/v^*$ estimated from horizontal profiles in the region of turbulence equilibrium, are respectively equal to 2.1, 1.3, and 1, which correspond to classical values in single phase flow wall turbulence.

The fluctuating velocity cross-correlation $\overline{v_x v_z}$ vertical profiles in L1 layer are reported in Figure 9 for both test cases. They are normalized by the friction velocity v^*, derived above. In both cases, the profiles exhibit two maxima of the absolute value of $\overline{v_x v_z}/v^{*2}$, below the interface and near the wall, then decrease towards zero at the wall and at the interface. Compared to the mean velocity profile of Figure 3, the crossing of vertical axis ($\overline{v_x v_z} = 0$) corresponds to the axial position of the maximum of longitudinal velocity. In the flow core ($5 < z < 25$ mm), the profile of $\overline{v_x v_z}$ is composed of two linear segments of different slopes. This peculiar shape is due to the flow structure asymmetry as depicted by the velocity contours in Figure 6a. Near the wall, contour shape is axisymetrical whereas it is nearly horizontal just below the interface. Neglecting in first approximation the weight of secondary flows, local momentum balance in the longitudinal direction reads:

$$\left(\overrightarrow{\nabla p}\right)\overrightarrow{e_x} = \left(\nabla.\bar{\bar{\tau}}\right)\overrightarrow{e_x} \tag{12}$$

In the wall region, the simplest form of (12) is obtained in cylindrical coordinates system:

$$\frac{\partial p}{\partial x} = \frac{1}{r}\frac{\partial}{\partial r} r\tau_{rx}, \quad \text{with } r = R - z \tag{13}$$

whereas below the interface, Cartesian coordinates are more appropriate:

$$\frac{\partial p}{\partial x} = \frac{\partial}{\partial z}\tau_{zx} \tag{14}$$

Integrating (13) and (14) over the vertical direction leads to:

$$\tau_{zx} = \frac{\partial p}{\partial x} z + cst \quad \text{above the wall} \tag{15}$$

and

$$\tau_{rx} = \frac{\partial p}{\partial x}\frac{z}{2} + cst \quad \text{below L1-L2 interface} \tag{16}$$

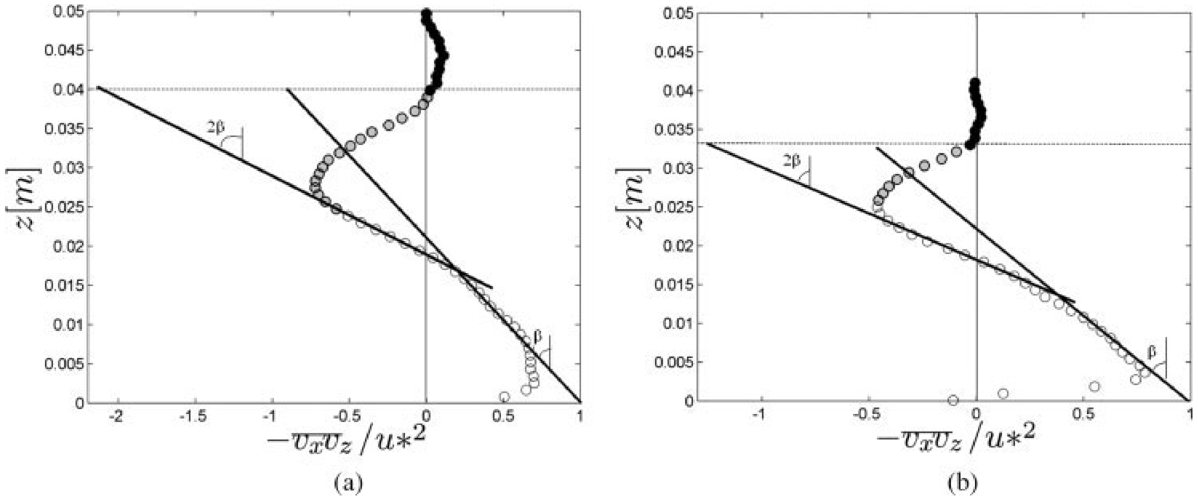

(a) (b)

Figure 9. Vertical profiles of velocity cross-correlation.

Horizontal line is the location of L1-L2 interface, z_I. $U_m = 0.57$ m/s. (a) $\phi_o = 0.1$; (b) $\phi_o = 0.2$.

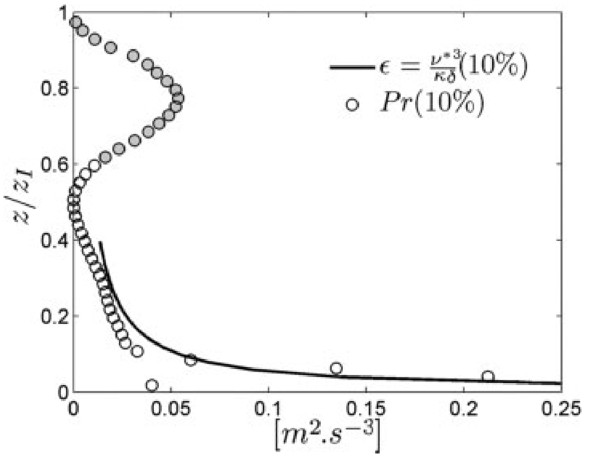

Figure 10. Vertical profiles of turbulence production and dissipation terms.

Hence, even if the tangential stress is assumed to be linear, Eqs. (15) and (16) show the existence of two distinct slopes due to the shape of velocity contours in L1 layer. The ratio between these two slopes is 0.5, in agreement with the experimental data (Figure 9).

Extension of the linear behavior of normalized cross-correlation profile near the wall tends towards unity (Figure 9), a result which validates the identification of the friction velocity v^* from the log-law profile, as well as the weak influence of secondary flows near the wall. In the transition zone (grey color symbols in Figure 9), the linear trend of cross-correlation profile no longer holds, suggesting a strong damping of the turbulence by the drop layer in that zone. Extension of the linear profile up to the interface can *a priori* be applied for the determination of the local interfacial stress. These results are discussed in last section.

In addition, from the vertical profile of Reynolds stress $\overline{v'_x v'_z}$ (Figure 9) and the vertical profile of longitudinal velocity $\overline{V_x}$ (Figure 3), the vertical profile of turbulent kinetic energy production can be determined. It is defined as follows:

$$\mathrm{Pr} = -\overline{v'_x v'_z}\frac{\partial \overline{V_x}}{\partial z} \tag{17}$$

In single phase flow, the production is balanced in the near wall region by the dissipation rate of turbulent kinetic energy. The dissipation rate is expected to vary with the distance to the wall δ as:

$$\varepsilon = \frac{v^{*^3}}{\kappa z} \tag{18}$$

Production and dissipation curves are reported in Figure 10 for the first test case. The two curves do well coincide in the near wall region, exhibiting classical turbulence equilibrium region.

Integral length scales of the fluctuating motion of the aqueous phase have been also calculated in the longitudinal direction from the autocorrelation function of the instant fluctuating velocity field. At a given distance z from the wall in a vertical median plane, these scales are defined as:

$$\Lambda_{xx}(z) = \frac{1}{\overline{v_x'^2(z)}}\int_0^\infty v'_x(x,z)v'_x(x+\lambda,z)\,dx$$

$$\text{and}\quad \Lambda_{xz}(z) = \frac{1}{\overline{v_z'^2(z)}}\int_0^\infty v'_z(x,z)v'_z(x+\lambda,z)\,dx \tag{19}$$

Evolutions of $\Lambda_{xx}(z)$ and $\Lambda_{xz}(z)$ are reported in Figure 11b. Close to the wall, they well compare with the classical trend observed in single phase turbulent pipe flow (straight line on the graph):

$$\Lambda = \frac{\kappa}{C_\mu^{3/4}}\delta \approx 2.5\,\delta \tag{20}$$

Overall, these results confirm that the aqueous phase flow possesses the main characteristics of single phase wall turbulence.

The production term (Figure 10) decreases in the neighborhood of the transition zone, then increases again, passes

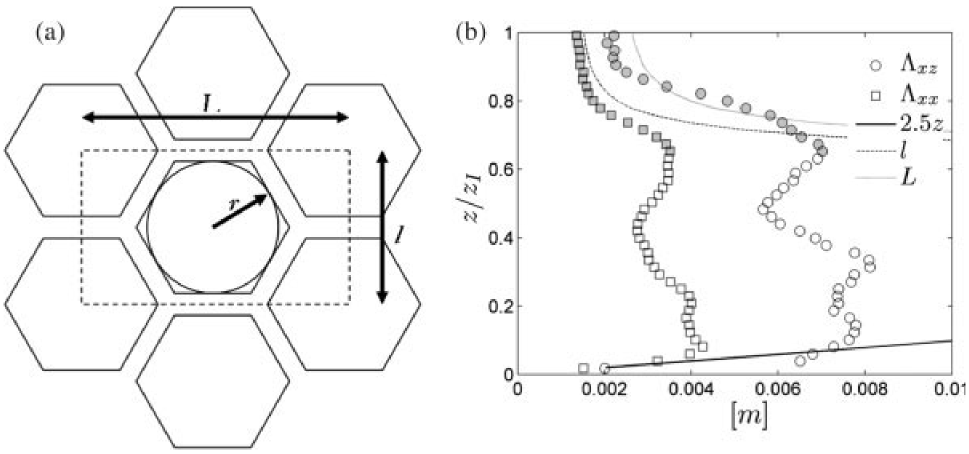

Figure 11. (a) 2-D representation of dispersed layer below z_I as a network of hexagons; (b) vertical profiles of integral (Λ_{xx} and Λ_{xz}) and geometrical (*l* and *L*) length scales; U_m = 0.57 m/s; ϕ_o = 0.1.

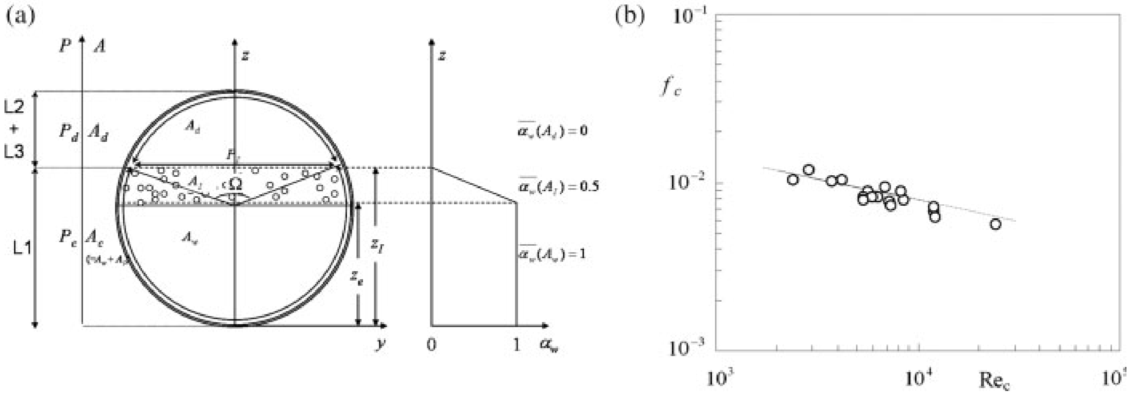

Figure 12. (a) Scheme of the stratified-dispersed flow cross-section and geometric parameters; (b) wall friction factor as a function of Reynolds number in layer L1.

Dashed line is Blasius law ($0.079Re_c^{-1/4}$).

through a local maximum and tends towards zero at $z = z_I$. This maximum corresponds to the maximum of velocity gradient in the transition zone (Figure 3), whereas the cross-correlation term continuously decreases ($z_e < z < z_I$). Integral length scales Λ_{xx} (z) and Λ_{xz} (z) of the fluctuating motion (Figure 11b) continuously decreases and tend towards constant values at the interface ($z = z_I$), and equal respectively to 1.3 and 2.2 mm. These length scales are related to the distribution of drops below the interface. Indeed, the drop phase fraction ($1 - \alpha_w$) increases from 0 in the single phase water region, up to almost 1 at the interface. The geometric length scales associated to the drop layer can be estimated considering the drop distribution can be approximated by a uniform network of hexagons (Figure 11a). The mesh size of this network is a rectangle of area A_N defined by two length scales l and L:

$$A_N = lL \tag{21}$$

The area of each hexagonal drop A_H is equal to:

$$A_H = \frac{\pi d^2}{4} = \frac{A_T}{2}(1 - \alpha_w) \tag{22}$$

The two characteristic length scales of the network are given by:

$$\frac{l}{d} = \left(\frac{\pi}{2\sqrt{3}(1-\alpha_w)}\right)^{1/2} \text{ and } \frac{L}{d} = \left(\frac{\pi\sqrt{3}}{2(1-\alpha_w)}\right)^{1/2} \tag{23}$$

The vertical profiles of $L/2$ and $l/2$ have been plotted in Figure 11b from the vertical profiles of the oil volume fraction ($1 - \alpha_w$) in the transition zone. Both profiles correctly fit the integral length scales profiles. It can be concluded that in the transition zone, the fluctuating motion results from drop relative motion in the dense layer and the contribution of turbulence is negligible.

Wall friction factor

The wall friction in the aqueous phase can be derived from the local measurements of the wall shear stress (Eq. 11), which has been shown to be constant along the wetted perimeter P_c:

$$f_c = \frac{2}{\rho_c}\frac{\overline{\tau_c}}{\overline{U_c}^2} \tag{24}$$

where $\overline{U_c}$ is the average velocity of the aqueous phase in the L1 layer. Note that due to the location of the interface z_I, $\overline{U_c}$ is not strictly equal to the continuous phase flowrate Q_c divided by the L1 section area A_c (flow cross-section area below z_I).

As illustrated in Figure 12a, aqueous phase cross-section flow is delimited by the interface position z_I and is composed of two sections: an emulsion zone of area A_I, comprised between z_I and z_e (the "first drop position"), and the section A_w below z_e and only occupied by the aqueous phase:

$$A_c = A_w + A_I \tag{25}$$

Above z_I, the volume ratio of aqueous phase in the dispersed layer is neglected ($\alpha_w = 0$, for $z_I < z < D$). The L2 area is noted A_d:

$$A = \pi R^2 = A_c + A_d = A_c + A_w + A_I \tag{26}$$

The mass balance for both phases therefore requires the concentration of each phase in the transition zone A_I. As shown in Figure 3, the local volume fraction α_w is not constant in that zone, but seems to vary linearly between $\alpha_w = 1$ at $z = z_e$ and $\alpha_w = 0$ at $z = z_I$. Hence, in that section, the average value of the aqueous phase can be approximated to 0.5:

$$\overline{\alpha_w} \cong 0.5 \quad \text{for } z_e < z < z_I \tag{27}$$

The average velocity $\overline{U_c}$ in L1 layer is given by:

$$\overline{U_c} \cong \frac{Q_w}{(A_w + A_I/2)} \tag{28}$$

Reynolds number in layer L1 is then defined as:

$$Re_c = \frac{\rho_c U_c D_{hc}}{\mu_c} \tag{29}$$

where μ_c and ρ_c are taken equal to the viscosity and the density of the aqueous phase respectively, and D_{hc} is the hydraulic diameter of section A_c:

$$D_{hc} = 4A_c/(P_c + P_I) \tag{30}$$

Note that all geometric parameters can be deduced from the location of the interface z_I. The wall friction factor f_c in the aqueous phase has been plotted in Figure 12b as a function of the Reynolds number Re_c. The data well regroup around Blasius law. Note that the proportion of water (up to 0.1) in layer L2 has little effect on the wall friction factor. However, this definition of the wall friction factor assumes the wall turbulence behavior is valid along the wetted perimeter of the aqueous phase, including the segment comprised between z_e and z_I.

Interfacial Shear Stress

Average interfacial stress

The average stress at the interface $\overline{\tau_I}$ is deduced from the macroscopic momentum balance in the L1 layer:

$$\overline{\tau_I} = \left(\frac{dp}{dx}A_c - \overline{\tau}_c P_c\right) \Big/ P_I \tag{31}$$

where dp/dx is the measured longitudinal pressure gradient.

Values of $\overline{\tau_I}$ deduced from Eq. 31 are reported in Table 2. As a first observation, the interfacial shear stress $\overline{\tau_I}$ has the same order of magnitude than the wall stress $\overline{\tau_c}$. In the 2-layer regime $\overline{\tau_I}/\overline{\tau_c}$ ratios are higher than 1 whereas in the 3-layer regime stress ratios are closer to 1. These results confirm the observed structure of secondary flows: in the first test case (U_m = 0.57 m/s, ϕ_o = 0.1, 2-layer regime), the interfacial friction is larger than the wall friction resulting in larger vortices along the wall than below the interface (Figure 5b). Whereas in the second test case (U_m = 0.57 m/s, ϕ_o = 0.2, 3-layer regime), the friction ratio being of the order of unity, vortices between the interface and the wall have similar sizes.

Following the analysis of wall friction, a friction factor can be defined at the interface:

$$f_i = \frac{2}{\rho_c}\frac{\overline{\tau_i}}{\overline{U_R^2}} \tag{32}$$

where $\overline{U_R} = \overline{U_w} - \overline{U_d}$ is the slip velocity between aqueous phase and dispersed phase. $\overline{U_w}$ is the average velocity of the aqueous phase below z_e and $\overline{U_d}$ the average velocity of the dispersed phase above z_I. $\overline{U_w}$ and $\overline{U_d}$ are derived from the mass balance. Taking the average velocity in the transition zone A_I as the arithmetic average of $\overline{U_w}$ and $\overline{U_d}$, it reads:

$$\left.\begin{aligned} \overline{U_d}A_d + \frac{1}{4}(\overline{U_d} + \overline{U_w})A_I = Q_o \\ \overline{U_w}A_w + \frac{1}{4}(\overline{U_d} + \overline{U_w})A_I = Q_w \end{aligned}\right\} \tag{33}$$

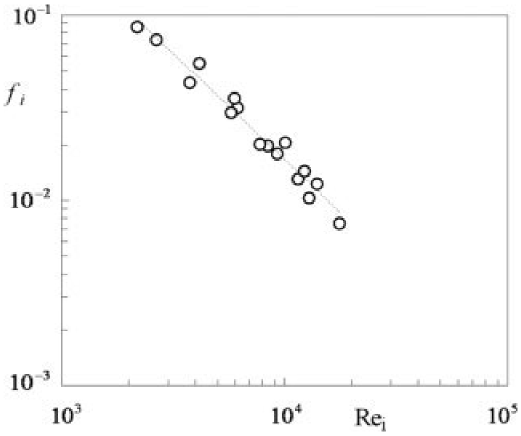

Figure 13. Interfacial friction factor as a function of Reynolds number.

Solutions of Eq. 33 are:

$$\overline{U_w} = \frac{[Q_w - A_I Q_d/4(A_d + A_I/4)]}{[A_w + A_I/4 - A_I^2/16(A_d + A_I/4)]}$$

$$\text{and } \overline{U_d} = \frac{Q_o - \overline{U_w}A_I/4}{A_d + A_I/4} \tag{34}$$

Interfacial Reynolds number Re_I is defined as follows:

$$Re_I = \frac{\rho_c \overline{U_R} D_{hc}}{\mu_c} \tag{35}$$

where D_{hc} is the hydraulic diameter. Combining (27), (28), (30), and (31) the interfacial friction factor has been plotted as a function of Re_i in Figure 13. The evolution follows a quasi-hyperbolic decay:

$$f_i \cong \frac{180}{Re_i} \tag{36}$$

This remarkable result clearly shows that despite the high values of the Reynolds number, due to the strong damping of turbulence below the interface, friction at the interface is entirely controlled by viscous effects. Compared to Hagen–Poiseuille law in a circular pipe (16/*Re*), the high value of the prefactor in Eq. 36 probably results from the fact that the viscosity to be accounted for in the Reynolds number should be the emulsion viscosity (which is probably significantly larger than the aqueous phase viscosity). Note also that the length scale to be considered below the interface is closer to the transition zone thickness (z_I-z_e) than to the hydraulic diameter D_{hc}.

Local shear stress near the interface

Two problems are addressed in this section. First of these concerns the determination of the local stress at the interface. As a first approximation, the local interfacial stress τ_{Iloc} may be estimated by extrapolating the linear behavior of the velocity cross-correlation profile below the transition zone up

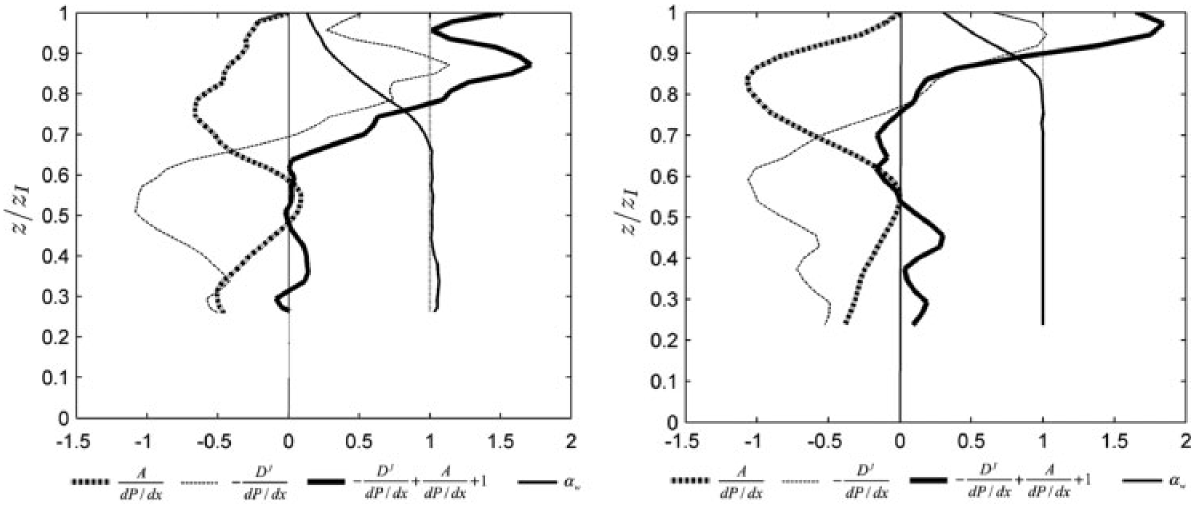

(a) (b)

Figure 14. Vertical profiles of advective and diffusive terms of momentum balance below the interface, with $\rho = \rho_c$ and $\mu = \mu_c$. $U_m = 0.57$ m/s; (a) $\phi_o = 0.1$; (b) $\phi_o = 0.2$.

to the interface, in the same way as the estimation of the wall shear stress (Figure 9). These values have been reported in Table 2 and can be compared to the mean interfacial stress deduced from the global momentum balance (see Eq. 31 above). Both quantities have the same order of magnitude, but local extrapolated values are always smaller than the average value. Such a trend is either due to an overestimation of in the transition zone or results from the influence of secondary flows in the transition zone. In that case, the linear behavior of the shear stress (Eq. 16) is no longer valid below the interface.

The second question is related to the identification of the local shear stress in the transition zone $z_e < z < z_I$. Because of the presence of a dense layer of drops distributed along a stiff vertical gradient of volume fraction, the evaluation of a local shear stress in that zone needs to consider the emulsion phase as a homogeneous flow with variable density and viscosity. The mean velocity and the velocity cross-correlation profiles being known (Figures 3 and 9), a local effective viscosity can be derived from the local momentum balance equation.

These two questions lead to first analyze the local momentum equation in the flow direction. In the aqueous phase, it reads:

$$\underbrace{\rho_c V_z \frac{\partial}{\partial z} V_x}_{A_v} - \underbrace{\frac{\partial}{\partial z}\left[\mu_c \frac{\partial V_x}{\partial z} - \rho_c \overline{v_x v_z}\right]}_{D^f} + \frac{dp}{dx} = 0 \tag{37}$$

Note that the advective term A_v (1st term of l.h.s. of (37)) is reduced to the vertical transport of longitudinal velocity. This simplification is only valid in the plane of symmetry where $V_y(y = 0) = 0$. In the diffusion term, the transversal gradient is neglected since near the transition zone, the velocity profile $V_x(y)$ is flat as well as the profile of cross correlation $\overline{v_x v_y}$ (y). The normalized advective and diffusive terms $\frac{A_v}{(dp/dx)}$ and $\frac{-D^f}{(dp/dx)}$ of (37) have been reported in Figure 14 as a function of the normalized vertical coordinate z/z_I, for both test cases. The vertical profile of the local volume fraction α_w is also displayed in these graphs (thin continuous line). Below z_e, the contribution of secondary flows to the momentum balance in the single phase flow region is significant but decreases towards the bottom of the pipe. These graphs show that the momentum balance (37) is correct below the transition zone (thick continuous line), whereas it abruptly increases for $z_e < z < z_I$, that is as soon as the local volume fraction of the aqueous phase begins to decrease. This behavior clearly suggests the existence of an effective viscosity μ much greater than that of the aqueous phase μ_c.

Introducing the dependence of the volume fraction in the density and viscosity, the integration of the momentum balance following z reads:

$$\begin{aligned}\tau(z) &= \mu(\alpha_w)\frac{\partial V_x}{\partial z} - \rho(\alpha_w)\overline{v_x v_z} \\ &= \int \rho(\alpha_w) V_z \frac{\partial V_x}{\partial z} dz + \left(\frac{dp}{dx}\right) z + cste\end{aligned} \tag{38}$$

The constant in Eq. 38 is determined at $z = z_e$ ($\alpha_w = 1$). The emulsion viscosity $\mu(\alpha_w)$ can therefore be deduced locally from (38). The evolution of μ/μ_c is displayed in Figure 15 for six different test cases. In this graph, the increase of α_w corresponds to a vertical displacement in the transition zone towards the interface. At "low" concentration of the dispersed phase ($0.4 < \alpha_w < 1$), the data well regroup on a single curve slightly above the Roscoe's law[21] valid for a suspension of spheres. At higher drop concentration ($0 < \alpha_w < 0.4$), the growth rate of the effective viscosity decreases and dispersion is observed between the different test cases. This result suggests that at high concentration, the drop deformation probably reduces the viscosity compared to a hard sphere suspension and that the dense dispersed layer can no longer be considered as Newtonian.

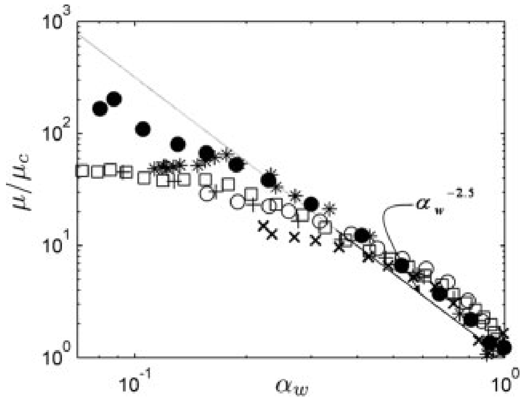

Figure 15. Effective viscosity as a function of the water volume fraction in layer L1.

Symbols: (○) $U_\mathrm{m} = 0.56$ m/s, $\phi_o = 0.1$; (●) U_m=0.56 m/s, $\phi_o = 0.2$; (x) $U_\mathrm{m} = 0.85$ m/s, $\phi_\mathrm{o} = 0.1$; (*) $U_\mathrm{m} = 0.56$ m/s, $\phi_\mathrm{o} = 0.3$; (☐) $U_\mathrm{m} = 0.28$ m/s, $\phi_\mathrm{o} = 0.3$; (+) U_m = 0.28m/s, $\phi_\mathrm{o} = 0.1$.$\alpha_\mathrm{w}^{-2.5}$ is the Roscoe's law (1952).

Finally, the shear stress can be evaluated at the interface ($z = z_\mathrm{I}$). The values (not reported here) are always smaller than τ_{Iloc} obtained from the extension of the linear part of the velocity cross-correlation profile below the interface (Figure 9). This difference is a direct consequence of effect of secondary flows (advective term) in the transition zone. As a result, it can be concluded that the local tangential stress at the interface is always smaller than the average value $\overline{\tau_\mathrm{I}}$ deduced from the macroscopic balance (Eq. 31). A possible explanation to this discrepancy is the contribution of the dispersed layer wall friction in the transition zone (that wets the wall segments of A_I) which is probably significantly larger than what is predicted by the Blasius law. Neglecting this effect leads to an underestimation of $\overline{\tau_\mathrm{c}}$ and as a consequence to an overestimation of $\overline{\tau_\mathrm{I}}$.

Conclusion

Hydrodynamic field of a dispersed-stratified liquid–liquid pipe flow has been investigated for a wide range of flow parameters (mixture velocity and inlet phase ratio). The mean and fluctuating velocity fields of the aqueous phase have been measured using PIV in a matched refractive index medium (*n*-heptane dispersed in water–glycerine mixture). The flow structure is composed of a continuous aqueous phase above which flows a dense layer of oil drops (2-layer regime). Depending on the oil inlet ratio, a third layer of continuous oil phase may also appear above the dense dispersed layer since the pipe entry (3-layer regime). PIV measurements have shown the presence of secondary flows from which the location of the interface between the aqueous phase and the dense dispersed layer has been determined. This interface does not correspond to the average position of the first drop but is located within the dispersed phase layer, bordering a zone where the aqueous phase volume ratio abruptly decreases from 1 to 0 (transition zone).

Analysis of mean and turbulent fields of the aqueous phase has shown that the classical logarithmic profile is valid and that the friction velocity along the aqueous phase wet perimeter is nearly uniform. In this zone below the transition zone, turbulence characteristics are close to those of single phase pipe flow. Despite the presence of secondary flows, wall friction factor verifies the classical Blasius law. With this definition of the interface position, a stratified two-phase momentum balance can be written to derive the average interfacial stress. It was shown that the interfacial friction factor is inversely proportional to the Reynolds number (based on an average slip velocity between the layers), suggesting a laminar behavior of the flow below the interface. This result is in agreement with a strong damping of turbulence below the interface and with the influence of an emulsion viscosity which increases as the aqueous phase volume fraction decreases in the transition zone.

This effective viscosity could be identified from the integration of the local momentum balance below the interface including the effect of the secondary flows (advective terms). Its evolution with the aqueous phase volume fraction suggests a non-Newtonian behavior at high concentration of the dispersed phase (larger than 0.6). The local shear stress at the interface has been also derived from the local momentum balance and was found to be always smaller than the average value deduced from the macroscopic balance. Local measurements have highlighted the flow complexity due to the development of secondary flows in all range of flow parameters investigated and to the rheology of the dispersion below the interface. The modeling of two-phase transport of this type of flow hence requires a finer description of the dispersion behavior below the interface. Finally, the study of the macroscopic momentum balance must be completed by the analysis of the dispersed layer wall stress above the interface. This work is under progress.

Literature Cited

1. Arirachakaran SKD, Oglesby MS, Malinovski MS, Shoham O, Brill JP. An analysis of oil/water flow phenomena in horizontal pipes. SPE paper 18836, SPE Production Operating Symposium. Oklahoma, March 13–14, 1989:155–167.
2. Nädler M, Mewes D. The effect of gas injection on the flow of two immiscibles liquids in horizontal pipes. *Chem Eng Technol*. 1995; 18:156–165.
3. Angeli P, Hewitt GF. Flow Structure in horizontal oil-water flow. *Int J Multiphase Flow*. 2000;26:1117–1140.
4. Elseth G. An experimental study of oil/water flow in horizontal pipes. PhD Thesis. Telemark University College, Porsgrunn, Norway, 2001.
5. Rodriguez OMH, Oliemans RVA. Experimental study on oil-water flow in horizontal and slightly inclined pipes. *Int J Multiphase Flow*. 2006;32:323–343.
6. Brauner N, Moalem Maron D. Flow pattern transitions in two-phase liquid–liquid flow in horizontal tubes. *Int J of Multiphase Flow*. 1992;18:123–140.
7. Trallero JL. Oil water flow patterns in horizontal pipes, PhD Dissertation, University of Tulsa, USA, 1995.
8. Brauner N. The prediction of dispersed flows boundaries in liquid–liquid and gas-liquid systems. *Int J of Multiphase Flow*. 2001;27: 885–910.
9. Chakrabarti DP, Das G, Das PK. The transition from water continuous to oil continuous flow pattern. *AIChE J*. 2006;52:3668–3678.
10. Liné A, Fabre J. Stratified flows, international encyclopedia of heat and mass transfer. *Innodata Corp*. 1996:1015–1021.
11. Raffel M, Willert C, Kompenhans J. *Particle image velocimetry, A practical guide*. Berlin: Springer-Verlag, 1998.

12. Fincham A, Delerce G. Advanced optimization of correlation imaging velocimetry algorithms. *Exp In Fluids [Suppl]*. 2000;29:13–22.
13. Laufer J. The structure of turbulence in fully developed pipe flow, Supersedes NACA TN 2954. Report 1174, 1954.
14. Augier F, Masbernat O, Guiraud P. Slip velocity and drag law in a liquid–liquid homogeneous dispersed flow. *AIChE J*. 2003;49:2300–2316.
15. Galinat S. Etude expérimentale de la rupture de gouttes dans un écoulement turbulent. Thèse INPT, Toulouse, France, 2005.
16. Adrian RJ. Particle-imaging techniques for experimental fluid mechanics. *Ann Rev Fluid Mech*. 1991;23:261–304.
17. Liné A, Masbernat L, Soualmia A. Interfacial interactions and secondary flows in stratified two-phase flow. *Chem Eng Commun*. 1996;141–142:303–329.
18. Meknassi F, Benkirane R, Liné A, Masbernat L. Numerical modeling of wavy stratified two-phase flow in pipes. *Chem Eng Sci*. 2000;55:4681–4697.
19. Hinze JO. Experimental investigation on secondary currents in the turbulent flow through a straight conduit. *Appl Sci Res*. 1975;28: 453–465.
20. Wang ZQ, Cheng NS. Secondary flows over artificial bed strips. *Adv Water Resour*. 2005;28:441–450.
21. Roscoe R. The viscosity of suspensions of rigid spheres. *Br J App Phys*. 1952;3:267–269.

Manuscript received Feb. 13, 2007, and revision received July 11, 2007.